

**Fig. 4.** The extent of conservation varies across brain regions. Patterns in neurochemistry are shown for the preoptic area (**top**) and striatum (**bottom**) where genes (rows) are either present (orange), absent (purple), or unknown (n/a, white) within each vertebrate lineage (columns). All other brain regions are shown in fig. S1.

Thus, our analysis provides a framework that will greatly facilitate the search for molecular universals underlying social behavior (30).

#### References and Notes

- L. A. O'Connell, H. A. Hofmann, *Front. Neuroendocrinol.* **32**, 320 (2011).
- S. W. Porges, *The Polyvagal Theory: Neurophysiological Foundations of Emotions, attachment, Communication, and Self-Regulation* (Norton, New York, 2011).
- G. F. Striedter, *Principles of Brain Evolution* (Sinauer, Sunderland, MA, 2005).
- A. A. Pollen, H. A. Hofmann, *Brain Behav. Evol.* **72**, 145 (2008).
- L. A. O'Connell, H. A. Hofmann, *J. Comp. Neurol.* **519**, 3599 (2011).
- S. W. Newman, *Ann. N.Y. Acad. Sci.* **877**, 242 (1999).
- J. L. Goodson, *Horm. Behav.* **48**, 11 (2005).
- K. C. Berridge, *Psychopharmacology (Berl.)* **191**, 391 (2007).
- J. R. Wickens, C. S. Budd, B. I. Hyland, G. W. Arbuthnott, *Ann. N.Y. Acad. Sci.* **1104**, 192 (2007).
- T. Dalglish, *Nat. Rev. Neurosci.* **5**, 583 (2004).
- A. B. Butler, W. Hodos, *Comparative Vertebrate Neuroanatomy: Evolution and Adaptation* (Wiley, New York, 1996).
- D. Crews, *Ann. N.Y. Acad. Sci.* **474**, 187 (1986).
- J. L. Goodson, R. R. Thompson, *Curr. Opin. Neurobiol.* **20**, 784 (2010).
- A. B. Butler, A. Reiner, H. J. Karten, *Ann. N.Y. Acad. Sci.* **1225**, 14 (2011).
- S. Kumar, S. B. Hedges, *Nature* **392**, 917 (1998).
- R. I. Wood, *Ann. N.Y. Acad. Sci.* **855**, 362 (1998).
- W. J. A. J. Smeets, O. Marín, A. González, *J. Anat.* **196**, 501 (2000).
- K. Yamamoto, J. O. Ruuskanen, M. F. Wullmann, P. Vernier, *J. Comp. Neurol.* **519**, 576 (2011).
- T. R. Insel, Z. X. Wang, C. F. Ferris, *J. Neurosci.* **14**, 5381 (1994).
- C. H. Leung *et al.*, *Endocrinology* **152**, 4865 (2011).
- A. G. Ophir, J. O. Wolff, S. M. Phelps, *Proc. Natl. Acad. Sci. U.S.A.* **105**, 1249 (2008).
- M. Chakraborty, S. S. Burmeister, *Horm. Behav.* **58**, 619 (2010).
- L. J. Young, P. K. Nag, D. Crews, *J. Neuroendocrinol.* **7**, 567 (1995).
- R. M. Harris-Warrick, *J. Comp. Physiol. A Neuroethol. Sens. Neural Behav. Physiol.* **186**, 605 (2000).
- A. Parent, D. Poitras, L. Dubé, in *Handbook of Chemical Neuroanatomy, Classical Transmitters in the CNS*, A. Björklund, T. Hökfelt, Eds. (Elsevier, Amsterdam, 1984), vol. 2, pp. 409–439.
- F. L. Moore, C. A. Lowry, *Comp. Biochem. Physiol. C Pharmacol. Toxicol. Endocrinol.* **119**, 251 (1998).
- Y. S. Kim, W. E. Stumpf, M. Sar, M. C. Martinez-Vargas, *Integr. Comp. Biol.* **18**, 425 (1978).
- O. Marín, J. L. Rubenstein, *Annu. Rev. Neurosci.* **26**, 441 (2003).
- S. B. Carroll, *Cell* **134**, 25 (2008).
- G. E. Robinson, R. D. Fernald, D. F. Clayton, *Science* **322**, 896 (2008).

**Acknowledgments:** The data reported in this paper are tabulated in the supplementary materials. We thank M. Cummings, S. Phelps, A. Pollen, M. Ryan, and R. Wong for helpful comments on earlier versions of this manuscript; members of the Hofmann laboratory, the Center for Brain, Behavior, and Evolution at UT Austin, and the Sociogenomics Initiative, especially G. Robinson, for discussions; and D. Canatella, E. Martins, and T. Streelman for advice on the evolutionary analysis. The work was supported by NSF Doctoral Dissertation Improvement Grant 1011253 to L.A.O. and NSF grant 0843712, the Alfred P. Sloan Foundation, a Dwight W. and Blanche Faye Reeder Centennial Fellowship in Systematic and Evolutionary Biology, and an Institute for Cellular and Molecular Biology Fellowship to H.A.H. The authors declare no competing financial interests. L.A.O. gathered all data for analysis; L.A.O. and H.A.H. conceived of the project, analyzed data, and wrote the paper.

**Supplementary Materials**  
[www.sciencemag.org/cgi/content/full/336/6085/1154/DC1](http://www.sciencemag.org/cgi/content/full/336/6085/1154/DC1)  
 Materials and Methods  
 Figs. S1 and S2  
 Tables S1 to S10  
 References (31–180)

9 January 2012; accepted 20 April 2012  
 10.1126/science.1218889

## Evolutionary Trade-Offs, Pareto Optimality, and the Geometry of Phenotype Space

O. Shoval,<sup>1</sup> H. Sheftel,<sup>1</sup> G. Shinar,<sup>1</sup> Y. Hart,<sup>1</sup> O. Ramote,<sup>1</sup> A. Mayo,<sup>1</sup> E. Dekel,<sup>1</sup> K. Kavanagh,<sup>2</sup> U. Alon<sup>1\*</sup>

Biological systems that perform multiple tasks face a fundamental trade-off: A given phenotype cannot be optimal at all tasks. Here we ask how trade-offs affect the range of phenotypes found in nature. Using the Pareto front concept from economics and engineering, we find that best-trade-off phenotypes are weighted averages of archetypes—phenotypes specialized for single tasks. For two tasks, phenotypes fall on the line connecting the two archetypes, which could explain linear trait correlations, allometric relationships, as well as bacterial gene-expression patterns. For three tasks, phenotypes fall within a triangle in phenotype space, whose vertices are the archetypes, as evident in morphological studies, including on Darwin's finches. Tasks can be inferred from measured phenotypes based on the behavior of organisms nearest the archetypes.

Consider a biological system whose phenotype is defined by a vector of traits,  $v$ . Traits considered here are quantitative measures such as bird beak length and not genetic traits such as DNA sequences. The space of all phenotypes is called the morphospace. Most theories of natural selection maximize a specific fitness function  $F(v)$ , resulting in an optimal phenotype, usually a point in morphospace. This approach has several limitations: First, the fitness function is often unknown. Second, in many cases, organisms need to perform multiple tasks that all contribute to fitness ( $I$ ); thus, fitness is

an increasing function of the performance at all tasks  $F(P_1(v), \dots, P_k(v))$ , where  $P_i(v)$  is the performance at task  $i$ . The best phenotype for one task is usually not the best for other tasks—resulting in a trade-off situation. Maximizing fitness is thus a multi-objective optimization problem (2–5).

To address this issue, we employ the Pareto front concept (2–6), used in engineering and economics to find the set of designs that are the best trade-offs between different requirements. Consider two phenotypes  $v$  and  $v'$ . If  $v'$  is better at all tasks than  $v$ , the latter will be eliminated by natural selection (Fig. 1A). Repeating this for all possible phenotypes, one remains with the Pareto front: the set of phenotypes that cannot be improved at all tasks at once. The Pareto front describes all optima for all conceivable fitness functions that are increasing functions of the

<sup>1</sup>Department of Molecular Cell Biology, Weizmann Institute of Science, Rehovot, Israel. <sup>2</sup>Biology Department, University of Massachusetts Dartmouth, Dartmouth, MA 02747, USA.

\*To whom correspondence should be addressed. E-mail: uri.alon@weizmann.ac.il

performance in each task. Which of the phenotypes on the front is selected depends on the relative contributions of each task to the organism's fitness in its natural habitat, provided that evolution has had sufficient time and genetic variance to reach the predicted point.

The Pareto front is typically a small region of morphospace. This may explain the long-standing observation that most of morphospace is empty (7): Phenotypes such as animal shapes found in nature fill only a small fraction of morphospace.

We next calculate the Pareto front in morphospace. This requires two assumptions (which will be relaxed below). (i) Each performance function is maximized by a single phenotype. The phenotype that is best at task  $i$  will be called the archetype for task  $i$ , denoted  $v_i^*$ . (ii) Performance decreases with distance from the archetype (Fig. 1B). By distance, we mean a metric based on an inner product norm, such as Euclidean distance [mathematically,  $P(v) = P(d_i)$ , where  $d_i = (v - v_i^*)^T M (v - v_i^*)$ , and  $M$  is a positive-definite matrix; Euclidean distance  $d_i = (v - v_i^*)^2$  is when  $M = I$ ]. For two tasks, geometric considerations show that the Pareto front is the line segment that connects the two archetypes (Fig. 1B). This is because any point off the line segment is farther from both archetypes than its projection on the line—thus points off the line have lower performance at both tasks, and hence lower fitness, and will be selected against. The position of a phenotype on the line relates to the relative importance of the two tasks in the habitat in which the organism evolved: the closer to an archetype, the more important that task (8).

The case of a trade-off between two tasks may explain the widespread occurrence of linear relations between traits (2, 9, 10). As an example, the area proportions of the molar teeth of 29 rodent species show an approximately linear relationship (11) (Fig. 1C). Species are distributed along the line according to their diet: herbivores at one end, carnivores at the other, and omnivores in the middle. Thus, the archetypes correspond to the ends of the observed line segment: a herbivore archetype with equal-sized molars, and a carnivore archetype with molars in the ratio 2:1:0. Omnivore molars are weighted averages of these archetypes. As in many morphological studies, the traits here are normalized to account for organism size: Because all molar areas scale with size, taking the ratio of molars removes the effect of organism size variation (8). Additionally, the present theory might explain cases of allometry, when traits depend on total organism size (9–12). Allometric relations often behave as power laws, observed as lines in logarithmic plots—predicted when the performance decays with a metric that is a function of the log of the traits (8), as suggested, for example, by scaling laws for metabolic transport (12). Other explanations for allometric relations include physical or developmental constraints (10, 11).

For more than two tasks, the Pareto front is the full polygon or polyhedron whose vertices are

the archetypes (8) (Fig. 2) [or, equivalently, the convex hull of the archetypes, defined as the set of all points that are weighted averages of the archetypes:  $v = \sum_{i=1}^k \theta_i v_i^*$  with nonnegative weights  $\theta_i$  that sum to one. For particular fitness and performance functions, the weights can be calculated:

$$\theta_i = \frac{\partial F}{\partial P_i} \frac{\partial P_i}{\partial d_i} / \sum_{j=1}^k \frac{\partial F}{\partial P_j} \frac{\partial P_j}{\partial d_j}. \text{Weights sum to one}$$

$\sum_{i=1}^k \theta_i = 1$ , and they are nonnegative,  $\theta_i \geq 0$ , because fitness increases with performance  $\partial F / \partial P_i \geq 0$  and performance decreases with distance from its archetype  $\partial P_i / \partial d_i < 0$  (8)]. For three tasks, the Pareto front is the full triangle whose vertices are the three archetypes. In this case, because a triangle defines a plane, even high-dimensional data on many traits are expected to collapse onto two dimensions. The closer a point is to one of the vertices of the triangle, the more important the corresponding task is to fitness in the organism's habitat.

We find evidence for such triangular suites of variation in several classic studies of animal morphology and evolution. In these studies, there was no theory to explain why the data resemble a

triangle. The species near the vertices of the triangles have distinct behavior that suggests which task is optimized by each archetype (Fig. 3, A to C). A triangle is found in the study of Grant and colleagues on Darwin's finches (13) (Fig. 3A). Measurements of five beak and body traits (five-dimensional morphospace) fall on a two-dimensional plane: Two principal components—related to body size and beak shape—account for 99% of the variation (8). On this plane, the data fall within a triangle [ $P < 10^{-4}$ , according to a statistical test of triangularity; Fig. 3A, inset (8, 14)]. The triangle suggests three archetypes, one at each vertex. The species near the archetypes suggest which tasks may be optimized by each archetype, in this case tasks connected with diet: (1) probing for insects and nectar (long beak, cactus finch), (2) crushing large, hard seeds (thick beak, large ground finch), and (3) crushing small, soft seeds (small beak, small ground finch). Intermediate finch species perform a combination of these tasks (8).

We also noted a triangle-shaped suite of variation in E. O. Wilson's study of leaf-cutter ants (15) [Fig. 3B,  $P < 10^{-4}$  (8, 14)]. The three

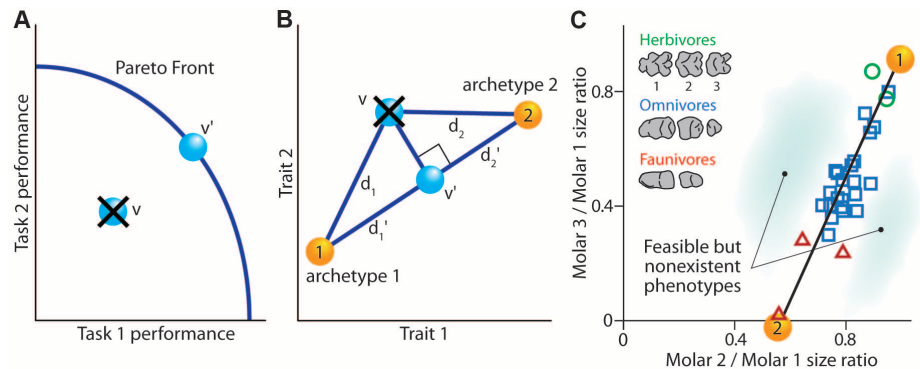


**Fig. 1.** (A) The Pareto front (best trade-offs) is what remains after eliminating (crossed-out symbol) all feasible phenotypes  $v$  that are dominated on all tasks by other feasible phenotypes  $v'$ . (B) The two archetypes in morphospace maximize performance in tasks 1 and 2. Phenotype  $v$  is farther from both archetypes than  $v'$ , its projection on the line segment that connects the archetypes. Thus,  $v$  has lower performance than  $v'$  in both tasks, hence lower fitness. Eliminating all such points  $v$ , one remains with the Pareto front: the line segment connecting the two archetypes [unlike (A), axes are traits, not performances]. (C) The area ratios of rodent molar areas show a linear relationship (11). Most of the morphospace is empty. Herbivores (circles), faunivores (triangles), and omnivores (squares) are indicated.

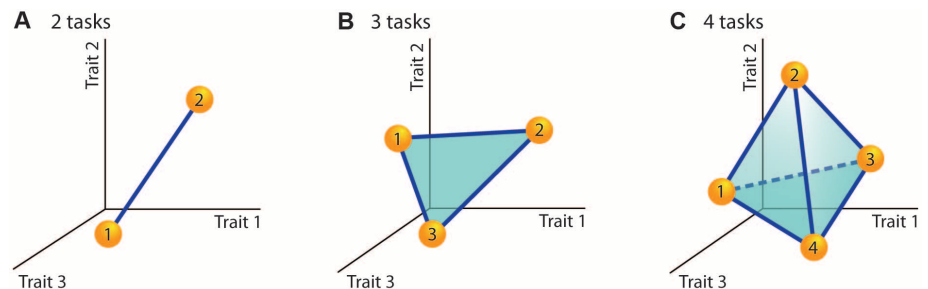


**Fig. 2.** Pareto front geometry. (A) Two tasks form a line (B) Three tasks form a triangle. (C) Four tasks form a tetrahedron. If only some relevant traits are measured and others are not, lines and triangles should still be found, because a projection of a convex hull on a subspace is still a convex hull (8). The distribution of phenotypes along the front depends on the second derivative of the performance and fitness functions (8).

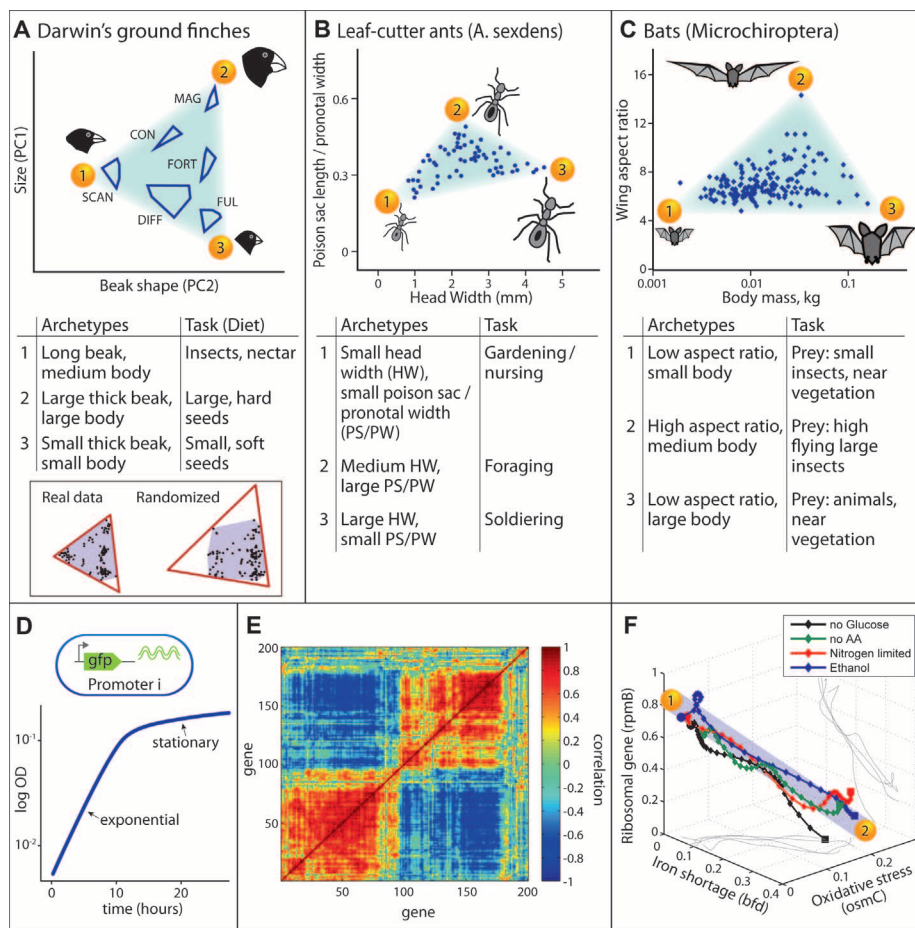
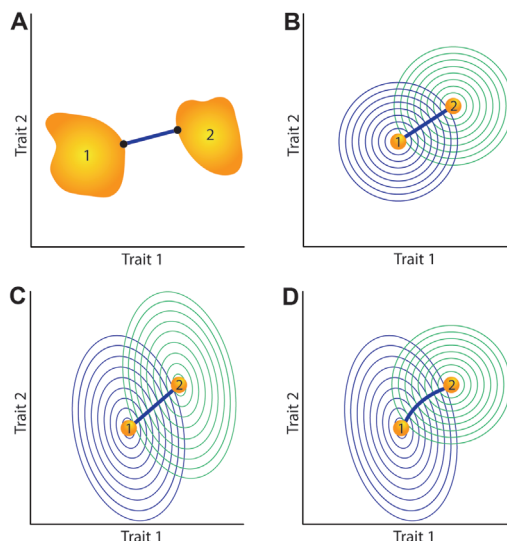


**Fig. 3.** Triangular suites of variation, and trade-offs in *E. coli* gene expression. **(A)** Darwin's ground finches (13). Axes correspond to size and beak shape. Polygons are boundaries of intraspecies variation. See (8) for species definitions. Inset: Statistical test for triangularity. Define  $t$  ratio as the ratio of the area of the minimal-area triangle (red) to the area of the convex hull of the data (purple). The  $P$ -value is the fraction of times that randomized data have a larger  $t$  ratio than the real data, based on  $10^4$  randomized data sets that preserve the statistics of each trait independently (8). **(B)** Leaf-cutter ant (*Atta sexdens*) (15): poison sac (pheromone gland that marks the trail) length (normalized to pronotal width) versus head width. **(C)** Bat (*Microchiroptera*) wing aspect ratio versus body mass (16). Archetypes and inferred tasks are listed below each figure. **(D)** *E. coli* promoter activity was measured with fluorescent reporters (18). **(E)** Clustered correlation matrix of the top 200 temporally varying genes reveals two anticorrelated clusters. **(F)** Percentage of total promoter activity of three genes at different time points, in four different media conditions (8), as bacteria transit from exponential phase (1) to stationary phase (2).

**Fig. 4.** **(A)** Relaxing assumption (i): When performance is maximized in a region rather than a single point, the Pareto front is the line that connects the closest point in the region to the other archetypes (8). **(B)** and **(C)** When all performance functions decay with the same distance metric, the Pareto front is a straight line. The front is the set of tangent points between equiprobability contours (8). **(D)** Relaxing assumption (ii): When each performance function decays with a different metric (different elliptical contours), the front is slightly curved. Root mean square deviation from a straight line is 21%, averaged over ellipses of all orientations and major/minor axis ratios spanning a hundredfold range (8). For three tasks, triangles with curved edges are generally found.



archetypes are associated with nursing/gardening, foraging outside the nest, and soldiering. Intermediate ants perform a combination of these tasks. Additionally, Norberg and Rayner's study of bat wings (16) [Fig. 3C,  $P < 3 \times 10^{-2}$  (8, 14)] shows a triangular pattern. Archetypes seem to be associated with eating insects in vegetation, hawking insects in the air far above vegetation, and eating large prey in vegetation.

The present considerations might apply beyond animal morphology. For example, bacteria face a trade-off in partitioning the total amount of proteins they can make at a given moment between the different types of proteins—that is, how much of each gene to express. A given expression pattern cannot be optimal, at the same time, for two different tasks such as rapid growth (which requires ribosomes) and survival (which requires stress response proteins) (17). Thus, the theory predicts that gene-expression patterns fall on low-dimensional Pareto fronts, whose vertices are archetypal expression patterns optimal for a single task.

We tested this hypothesis on *Escherichia coli* gene expression (Fig. 3D). The activity of 1600 promoters was tracked with fluorescent reporters as bacteria grew from exponential to stationary phase (18). Activity was normalized by the summed activity of all promoters at each time point, to represent the instantaneous allocation of transcription resources. The top 200 temporally varying promoters account for 96% of the total temporal variation and control genes in two main families (Fig. 3E) (8): growth genes (ribosomes, transcription, and translation) and stress/survival genes (oxidative stress, etc.). This high-dimensional data set falls on a line [Fig. 3F,  $P < 10^{-4}$  (8), fig. S10]. At one end, expression is devoted mostly to growth genes (exponential phase, archetype 1), and at the other end expression is devoted primarily to stress/survival genes (stationary phase, archetype 2). Over time, the expression program gradually moves along the line from archetype 1 to 2. The instantaneous allocation at each time point is, to a good approximation, a weighted average of two archetypal expression programs: growth and survival. Similar analysis may explain low-dimensional patterns in gene-expression measurements in bacteria (19) and cancer cells (20).

Relaxing the assumptions (i) and (ii) above generally preserves the topology of the Pareto front, with mildly curved lines instead of straight edges, but nevertheless with distinct vertices that can be related to archetypes (Fig. 4) (8).

The present theory addresses traits that have a trade-off. If a trade-off does not exist, trait values can vary independently. Observed phenotypes in this case may fill an uncorrelated cloud in morphospace (8).

Variation in traits within a population in a given species often falls on the same line as variations between species—a phenomenon called “evolution along genetic lines of least resistance” (21). This can be explained by the present frame-



work: Variation within a species reflects the range of habitats it inhabits, each with differential importance of the tasks. Thus, populations should be distributed on the same Pareto front as different species facing the same tasks.

Finally, Pareto optimality need not be the only or generic explanation for low dimensionality and lines/triangles in biological data. It may work for some examples and not others, especially if biological constraints other than natural selection are important. The following experimental tests can refute the theory in a specific example: (i) A point in the middle of the front has higher performance in one of the tasks than a point close to the relevant vertex (this might also imply that different tasks are at play). (ii) A mutant can be found that has higher performance at all tasks than existing phenotypes. Both of these tests require measuring performance (*I*, 7, 13)—but not the more difficult task of measuring fitness. (iii) Laboratory evolution experiments can follow a mutant that is off the Pareto front (has lower performance in all tasks than the wild type), under conditions in which all tasks are required. Provided with sufficient genetic variation, the

mutant is predicted to evolve phenotypes closer to the front.

#### References and Notes

1. S. J. Arnold, *Am. Zool.* **23**, 347 (1983).
2. G. F. Oster, E. O. Wilson, *Caste and Ecology in the Social Insects* (Princeton Univ. Press, Princeton, NJ, 1979).
3. K. D. Farnsworth, K. J. Niklas, *Funct. Ecol.* **9**, 355 (1995).
4. H. El Samad, M. Khammash, C. Homesu, L. Petzold, Optimal performance of the heat-shock gene regulatory network, *Proc. 16th IFAC World Congress* (2005).
5. M. C. Kennedy, *Ecol. Res.* **25**, 723 (2010).
6. R. E. Steuer, *Multiple Criteria Optimization: Theory, Computation, and Application* (Wiley, New York, 1986).
7. G. R. McGhee, *The Geometry of Evolution: Adaptive Landscapes and Theoretical Morphospaces* (Cambridge Univ. Press, Cambridge, 2007).
8. Supplementary materials are available on Science Online.
9. S. J. Gould, *Biol. Rev. Camb. Philos. Soc.* **41**, 587 (1966).
10. C. P. Klingenberg, *Nat. Rev. Genet.* **11**, 623 (2010).
11. K. D. Kavanagh, A. R. Evans, J. Jernvall, *Nature* **449**, 427 (2007).
12. G. B. West, J. H. Brown, B. J. Enquist, *Science* **276**, 122 (1997).
13. P. R. Grant, I. Abbott, D. Schluter, R. L. Curry, L. K. Abbott, *Biol. J. Linn. Soc. Lond.* **25**, 1 (1985).
14. Software that analyzes data in terms of triangles and their significance, and suggests archetype trait values, is available at [www.weizmann.ac.il/mcb/UriAlon](http://www.weizmann.ac.il/mcb/UriAlon).
15. E. O. Wilson, *Behav. Ecol. Sociobiol.* **7**, 143 (1980).
16. U. M. Norberg, J. M. V. Rayner, *Philos. Trans. R. Soc. Lond. B Biol. Sci.* **316**, 335 (1987).
17. T. Nyström, *Mol. Microbiol.* **54**, 855 (2004).
18. A. Zaslaver *et al.*, *PLOS Comput. Biol.* **5**, e1000545 (2009).
19. M. Scott, C. W. Gunderson, E. M. Mateescu, Z. Zhang, T. Hwa, *Science* **330**, 1099 (2010).
20. N. Geva-Zatorsky *et al.*, *Cell* **140**, 643 (2010).
21. D. Schluter, *Evolution* **50**, 1766 (1996).

**Acknowledgments:** We thank N. Barkai, R. Milo, O. Feinerman, C. Tabin, J. Losos, M. Khammash, T. Dayan, and N. Ulanovski for discussion. U.A. holds the Abisch-Frenkel Professorial Chair; O.S. is an Azrieli Fellow. This work was supported by the Israel Science Foundation and the European Research Council (FP7).

#### Supplementary Materials

[www.sciencemag.org/cgi/content/full/science.1217405/DC1](http://www.sciencemag.org/cgi/content/full/science.1217405/DC1)  
Materials and Methods  
Figs. S1 to S24  
Table S1  
References (22–46)

2 December 2011; accepted 6 April 2012  
Published online 26 April 2012;  
10.1126/science.1217405

## Chitin-Induced Dimerization Activates a Plant Immune Receptor

Tingting Liu,<sup>1,2,3,4,\*</sup> Zixu Liu,<sup>4,5\*</sup> Chuanjun Song,<sup>6</sup> Yunfei Hu,<sup>7,8</sup> Zhifu Han,<sup>2,3</sup> Ji She,<sup>8</sup> Fangfang Fan,<sup>6</sup> Jiawei Wang,<sup>3</sup> Changwen Jin,<sup>7,8</sup> Junbiao Chang,<sup>6,†</sup> Jian-Min Zhou,<sup>4,9,†</sup> Jijie Chai<sup>2,3,†</sup>

Pattern recognition receptors confer plant resistance to pathogen infection by recognizing the conserved pathogen-associated molecular patterns. The cell surface receptor chitin elicitor receptor kinase 1 of *Arabidopsis* (AtCERK1) directly binds chitin through its lysine motif (LysM)—containing ectodomain (AtCERK1-ECD) to activate immune responses. The crystal structure that we solved of an AtCERK1-ECD complexed with a chitin pentamer reveals that their interaction is primarily mediated by a LysM and three chitin residues. By acting as a bivalent ligand, a chitin octamer induces AtCERK1-ECD dimerization that is inhibited by shorter chitin oligomers. A mutation attenuating chitin-induced AtCERK1-ECD dimerization or formation of nonproductive AtCERK1 dimer by overexpression of AtCERK1-ECD compromises AtCERK1-mediated signaling in plant cells. Together, our data support the notion that chitin-induced AtCERK1 dimerization is critical for its activation.

In plants, pathogen-associated molecular pattern (PAMP)-induced immunity is mediated by the typically membrane-anchored proteins (1–3) pattern recognition receptors (PRRs), most of which are receptor-like kinases (RLKs) (4). Several PRRs (5–9) have been identified, including those critical for chitin-induced immune responses. Chitin, a polymer of *N*-acetyl-D-glucosamine (NAG), is a well-known PAMP that elicits plant immunity (10). The first chitin receptor identified in rice (*Oryza sativa*), OsCEBiP (9), carries an extracellular lysine motif (LysM) domain that is widely distributed for NAG recognition (11). In *Arabidopsis*, a CEBiP homolog, AtCERK1 (5) or LysMRLK1 (6), is required for chitin-triggered immunity. LysM-containing receptors appear to have a conserved role in

chitin perception, as they also contributed to chitin-induced plant defenses in other species (12, 13). AtCERK1 is also involved in detecting the bacteria-derived peptidoglycans (PGNs) to mediate *Arabidopsis* immunity (14, 15). Besides plant defenses, LysM-containing proteins recognize the chitin-related molecules, Nod factors, to initiate root nodulation (16).

AtCERK1 has been established as a chitin receptor (5, 6, 17, 18), and the AtCERK1-ECD containing three tandem LysMs (LysM1–3) directly recognizes chitin to signal plants for immunity (17, 18). Chitin binding induces phosphorylation of the intracellular kinase domain of AtCERK1 (17) and activates disease resistance (5, 6, 10, 19, 20). Here we present biochemical, molecular, and structural data (table S1) supporting a model in

which chitin-induced oligomerization is important for AtCERK1 activation, providing a template for understanding PAMP-induced PRR activation.

The three LysMs pack tightly against each other, resulting in a globular structure. Each LysM contains a  $\beta\alpha\alpha\beta$  structure in which the two  $\beta$  strands form an antiparallel  $\beta$  sheet (Fig. 1). The three LysMs share a conserved architecture (fig. S1A) that is similar to those of other LysM-containing proteins (fig. S2). The comparatively conserved residues among the three LysMs are limited to the  $\beta\alpha\alpha\beta$  regions (fig. S1B). Though making few contacts with each other, LysM2 and LysM3 pack tightly against LysM1.  $\beta$ 1 in LysM1 and its counterpart  $\beta$ 5 in LysM3 form a parallel  $\beta$  sheet, relating the two LysMs in a quasi two-symmetry axis (Fig. 1, left). LysM1 and LysM2 are also related by a quasi two-symmetry axis but through packing of different structural elements (Fig. 1, right). The tight packing of the three LysMs suggests that deletion of one LysM could

<sup>1</sup>Graduate Program in Chinese Academy of Medical Sciences and Peking Union Medical College, Beijing 100730, China.

<sup>2</sup>Tsinghua-Peking Center for Life Sciences, Beijing 100084, China.

<sup>3</sup>School of Life Sciences, Tsinghua University, Beijing 100084, China.

<sup>4</sup>National Institute of Biological Sciences, No. 7 Science Park Road, Beijing 102206, China.

<sup>5</sup>School of Life Science, Nanjing University, Nanjing 210093, China.

<sup>6</sup>Department of Chemistry, Zhengzhou University, Zhengzhou 450001, China.

<sup>7</sup>Beijing NMR Center, Peking University, Beijing 100871, China.

<sup>8</sup>College of Life Sciences, Peking University, Beijing 100871, China.

<sup>9</sup>State Key Laboratory of Plant Genomics and National Center for Plant Gene Research, Institute of Genetics and Developmental Biology, Chinese Academy of Sciences, Beijing 100101, China.

\*These authors contributed equally to this work.  
†To whom correspondence should be addressed: [chaijj@mails.tsinghua.edu.cn](mailto:chaijj@mails.tsinghua.edu.cn) (J.Chai); [jmzhou@genetics.ac.cn](mailto:jmzhou@genetics.ac.cn) (J.-M.Z.); [changjunbiao@zju.edu.cn](mailto:changjunbiao@zju.edu.cn) (J.Chang)